PROCEEDINGS OF SPIE

SPIEDigitalLibrary.org/conference-proceedings-of-spie

Plasmonic and photonic isolators based on the spatiotemporal modulation of graphene

D. Correas-Serrano, N. K. Paul, J. S. Gomez-Diaz

D. Correas-Serrano, N. K. Paul, J. S. Gomez-Diaz, "Plasmonic and photonic isolators based on the spatiotemporal modulation of graphene," Proc. SPIE 10982, Micro- and Nanotechnology Sensors, Systems, and Applications XI, 109821I (13 May 2019); doi: 10.1117/12.2519237

SPIE.

Event: SPIE Defense + Commercial Sensing, 2019, Baltimore, Maryland, United States

Invited Paper

Plasmonic and Photonic Isolators based on the Spatiotemporal Modulation of Graphene

D. Correas-Serrano, N. K. Paul, J. S. Gomez-Diaz*
Department of Electrical and Computer Engineering, University of California Davis, one Shields Avenue, Kemper Hall 2039, Davis, California 95616, USA
*jsgomez@ucdavis.edu

ABSTRACT

We explore the possibilities enabled by the spatiotemporal modulation of graphene's conductivity to realize magnetic-free isolators at terahertz and infrared frequencies. To this purpose, graphene is loaded with periodically distributed gates that are time-modulated. First, we investigate plasmonic isolators based on various mechanisms such as asymmetric bandgaps and interband photonic transitions and we demonstrate isolation levels over 30 dB using realistic biasing schemes. To lessen the dependence on high-quality graphene able to support surface plasmons with low damping, we then introduce a hybrid photonic platform based on spatiotemporally modulated graphene coupled to high-Q modes propagating on dielectric waveguides. We exploit transversal Fabry-Perot resonances appearing due to the finite-width of the waveguide to significantly boost graphene/waveguide interactions and to achieve isolation levels over 50 dB in compact structures modulated with low biasing voltages. The resulting platform is CMOS-compatible, exhibits an overall loss below 4 dB, and is robust against graphene imperfections. We also put forward a theoretical framework based on coupled-mode theory and on solving the eigenstates of the modulated structure that is in excellent agreement with full-wave numerical simulations, sheds light in the underlying physics that govern the proposed isolators, and speeds-up their analysis and design. We envision that the proposed technology will open new and efficient routes to realize integrated and silicon-compatible isolators, with wide range of applications in communications and photonic networks.

Keywords: Nonreciprocity, graphene, plasmonics, photonics, isolators, waveguides, terahertz, infrared.

I. INTRODUCTION

Recent years have witnessed growing interest in breaking the reciprocity of electromagnetic devices without relying on magneto-optic effects by imparting linear or angular momentum to the supported waves. This spatiotemporal modulation scheme has proven itself useful to develop a wide variety of nonreciprocal devices [1], such as circulators [2-4], isolators [5-10], filters [11,12], and antennas [13-15]. Unfortunately, as frequency increases, the challenges to implement this technique in practice also increase due to the difficulty to modify the properties of materials operating in terahertz, infrared and visible frequencies with enough speed [1, 16-18]. As a result, the quest for magnetic-free, integrated, and efficient magnetless nonreciprocal devices in these frequency bands continues.

In this work, we explore the possibilities offered by graphene [19, 20] to realize plasmonic and photonic isolators at terahertz and infrared frequencies by implementing spatio-temporal modulation approaches [21,22]. Graphene is very well-suited for this task because (i) its conductivity can be modulated with very high speed [23]; (ii) it intrinsically supports confined surface plasmons polaritons (SPPS) with many attractive features [19, 20, 24-26] and (iii) it is compatible with CMOS technology. In the following, we investigate nonreciprocal plasmons supported by graphene by simultaneously modulating its conductivity in space and time via time-varying gate voltages. This configuration imparts linear momentum to the SPPs traveling along the structure, breaking time reversal symmetry and thus reciprocity [1]. Several mechanisms are considered, including engineering asymmetric bandgaps and enforcing interband photonic transitions between orthogonal modes. The main technological challenges in the practical realization of these devices include (i) the fabrication of gating pads with an RC constant small enough to allow fast modulation of graphene's conductivity; and (ii) availability of high-quality graphene for overall low loss. Fortunately, the state of the art is advancing rapidly, with (i) sufficiently fast modulations recently achieved (speeds greater than 30 GHz have already been experimentally reported [23]); and (ii) low-loss SPPs has been observed in h-BN encapsulated graphene [27] with effective relaxation times greater than 0.5 ps.

To lessen even further the reliance on graphene's quality, we propose an alternative technological platform that combines the ultra-fast modulation speed enabled by graphene with high-quality factor photonic modes in dielectric waveguides,

Micro- and Nanotechnology Sensors, Systems, and Applications XI, edited by Thomas George, M. Saif Islam, Proc. of SPIE Vol. 10982, 109821I · © 2019 SPIE
CCC code: 0277-786X/19/$18 · doi: 10.1117/12.2519237

exploiting the most attractive features of each configuration. The resulting hybrid graphene-dielectric isolator is low-loss, silicon compatible, robust against fabrication tolerances, and scalable in frequency [22]. In contrast with our recent work that considered slabs with infinite width [22], here we take advantage of the transverse Fabry-Perot resonances that appear by controlling the waveguide finite width to maximize the coupling between graphene and the photonic mode, which permits us to significantly increase the achievable isolation, reduce the overall dimensions of the device, and simplify the biasing scheme. Finally, we briefly describe a theoretical framework based on coupled-mode theory and on solving the eigenstates of different structures to illustrate the physical mechanisms that govern spatiotemporally modulated graphene. Full-wave numerical simulations from COMSOL Multiphysics are employed to validate our theory. We emphasize that this platform outperforms other solutions available in the infrared and terahertz band to develop isolators [9, 28] and may pave the way towards silicon-compatible fully-planar nonreciprocal plasmonic technology at terahertz and infrared frequencies, with important applications in biosensing, imaging, and intra/inter-chip communications.

II. PLASMONIC ISOLATOR BASED ON ASSYMTRETRIC BANDGAPS

Let us consider the simplest structure one could envision to spatiotemporally modulate graphene's conductivity: a single sheet of this 2D material with various gating pads underneath, to which voltages oscillating in time with different phases are applied, as shown in Fig. 1a. The carrier density n_s in the graphene area above each gating electrode is approximately given by [29]

$$C_{ox}(V_i - V_{Dirac}) = q_e n_s, \tag{1}$$

where V_i is the voltage applied to the i[th] electrode, V_{Dirac} is the voltage at the Dirac point, $-q_e$ is the electron charge, and $C_{ox} = \varepsilon_r \varepsilon_0 / h$, where ε_r is the insulator relative permittivity and h is the distance between the gate and graphene. The

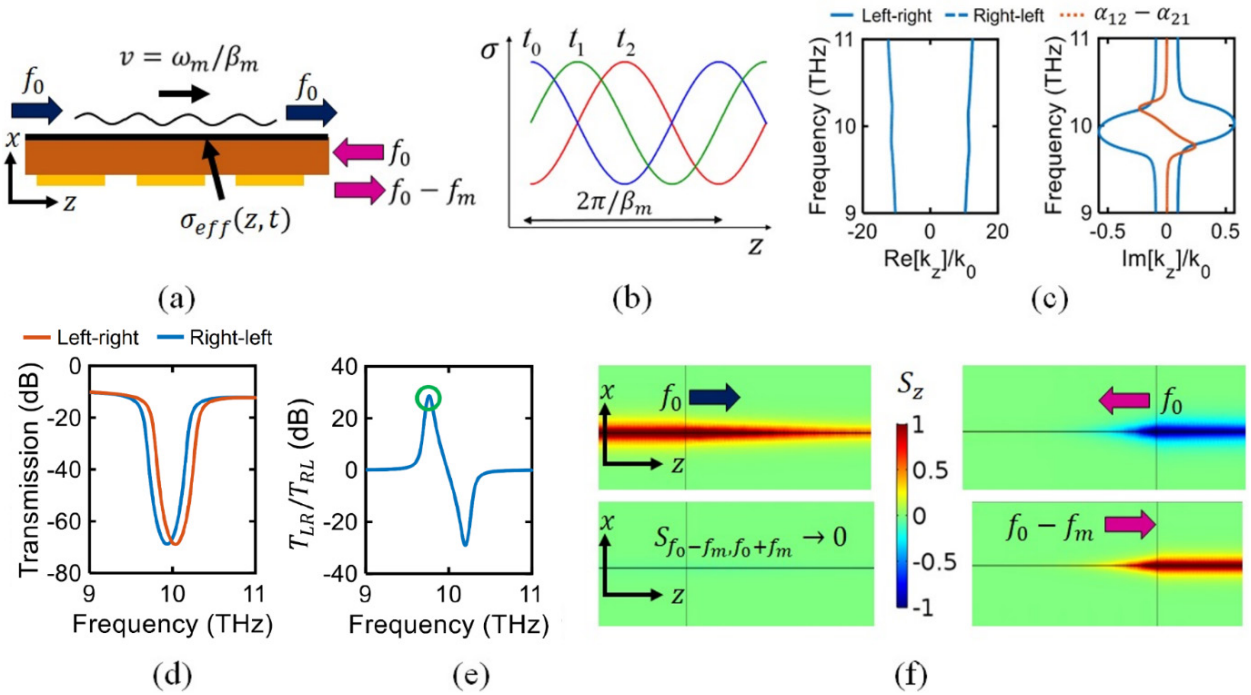

Figure 1. Graphene plasmonic isolator based on asymmetric bandgap. (a) Schematic of a waveguide composed of spatiotemporally modulated graphene. Graphene's conductivity is controlled along the z-axis using gating pads (in yellow) that are time-modulated, leading to an effective conductivity profile $\sigma_{eff}(\omega, z, t)$. (b) Resultant conductivity profile along the z-direction for three different time instants: t_0, $t_1 = t_0 + 1/(4f_m)$, and $t_2 = t_0 + 1/(2f_m)$, where f_m is the modulation frequency. As a result, the conductivity profile appears to travel in wave-like form toward $+z$, imparting linear momentum to the supported SPPs. (c) Real and imaginary part of the wavenumber of the fundamental harmonic near the bandgap. (d) Transmission through the structure when excited from left and right ports. (e) Contrast between the transmissions in both directions. (f) Full-wave simulation of the isolator's response for the frequency of maximum transmission contrast, marked by a green circle in panel (e). Graphene's chemical potential is $\mu_c = 0.25$ eV, relaxation time is $\tau = 1$ ps, $M = 0.1$, $\omega_m = 2\pi \times 80$ GHz, $\beta_m = 4.73 \times 10^6$ (rad/m) and device length is 65 μm.

relationship between the carrier density and the chemical potential μ_c can be found in the literature [19]. For moderately doped graphene ($|\mu_c| \gg k_B T$, with k_B being the Boltzmann constant and T the temparature) and below the interband transition threshold ($\hbar\omega < 2|\mu_c|$, with $\hbar$ being the reduced Planck's constant), graphene conductivity follows a Drude dispersion, which for convenience can be written as

$$\sigma(\omega) = \frac{\sigma_s}{1 + j\omega\tau}, \tag{2}$$

where $\sigma_s = q_e^2 \mu_c / (\hbar^2 \pi)$ is the Drude weight, equal to the conductivity at DC ($\omega = 0$), and τ is graphene's phenomenological relaxation time. Within this model, which is typically valid at terahertz and far infrared frequencies, changes in the chemical potential translate linearly into variations of σ_s, independently of frequency. This allows studying the influence of time-varying biasing voltages on graphene conductivity without neglecting the intrinsic frequency dispersion of graphene, given by the denominator of Eq. (2). With the modulation of Fig. 1a, graphene's effective conductivity looks like a wave travelling along the *z*-axis as

$$\sigma_{eff}(z,t) \approx \sigma(\omega) \cdot (1 + M\, cos[\omega_m t - \beta_m z]), \tag{3}$$

where *M* is the modulation depth, ω_m is the modulation frequency, and $\beta_m = 2\pi/p$ is the modulation wavenumber with p being the spatial period. Note that, because the voltage variation across adjacent pads is small, the assumption of smoothness implicit above is valid at every time instant [30,31]. Fig. 1b shows the conductivity profile along the graphene waveguide for different time instants, illustrating the wave-like nature that enables the exotic responses presented in the following.

The structure considered in Fig. 1a allows to implement a plasmonic isolator if the modulation parameters are correctly chosen. It is well known that a spatially periodic perturbation to a waveguide introduces bandgaps in which the propagation constant acquires an imaginary part associated to reflection [22,32], which is the operation principle behind Bragg gratings [22]. The proposed isolator works on a similar principle, but the time-varying behavior of the perturbation asymmetrically flips the frequency-shifts of the bandgaps for left to right and right to left propagation. Without applying any modulation, it is very well known that graphene supports transverse-magnetic (TM) SPPs. It is therefore expected that the device under study will support TM SPPs with an infinite number of spatial and temporal harmonics, as the modulation makes the structure periodic in both domains. The field of the guided modes above and below the graphene sheet may therefore be expressed as

$$\begin{aligned} H_x^{up} &= \sum_{i=-\infty}^{\infty} A_i e^{j\omega_i t} e^{-jk_{y1} y} e^{-jk_{zi} z}, \\ H_x^{down} &= \sum_{i=-\infty}^{\infty} B_i e^{j\omega_i t} e^{-jk_{y1} x} e^{+jk_{zi} z}, \end{aligned} \tag{4}$$

where $k_{yni} = \sqrt{\varepsilon_{rn} k_{0i}^2 - k_{zi}^2}$ is the *y*-component of the wavenumber in the medium *n* with permittivity ε_{rn}, for the i^{th} harmonic, *A* and *B* are arbitrary amplitude constants, $\omega_i = \omega_0 + i\omega_m$, the graphene sheet is located at $y = 0$, and the $e^{j\omega t}$ time convention has been followed. The associated electric field is given by Maxwell's equations. Enforcing continuity of the tangential fields across the interfaces and using the boundary condition on graphene $\hat{n} \times (\vec{H}_1 - \vec{H}_2) = \sigma_{eff}(z,t)\vec{E}_t$, the general dispersion relation of the modulated structure for an arbitrary number of harmonics can be found [33]. For a free-standing graphene sheet, it yields

$$\frac{M}{4} Z_{yi-1} A_{i-1} + \left(\frac{1 + j\omega_i \tau}{\sigma(\omega_i)} + \frac{1}{2} Z_{yi} \right) A_i + \frac{M}{4} Z_{yi+1} A_{i+1} = 0, \tag{5}$$

where $Z_{yi} = \frac{k_{yi}}{\omega_i \varepsilon_0}$. Eq. (5) can be solved for k_{yi} and thus k_{zi} through a continuous fraction method or by truncation in matrix form and solving the determinant [33]. From this, the amplitude of the different harmonics can also be found as the eigenfunctions of the corresponding eigenvalues [34].

Fig. 1c studies the response of this type of isolator, illustrating how the bandgaps are split in frequency by ω_m for the two propagation directions. There are thus excitation frequencies where the plasmons decay much faster in one direction due to back-scattering, and arbitrarily high contrast between transmission for both excitation directions can be realized by

making the structure as long as necessary –this also increases insertion loss in the 'non-isolated' direction, so a clear trade-off exists between insertion loss and isolation. Panel (d) shows the transmission for a device length of 65 μm, and panel (e) shows the transmission contrast, or isolation. Importantly, different ports are isolated at different frequencies. Panel (f) shows the z-component of the poynting vector, computed in COMSOL Multiphysics using harmonic balance simulations for the operation point highlighted by the green circle in (e), confirming the predicted response. To analyze the structure in COMSOL, coupling between adjacent harmonics is introduced through surface currents on graphene, with magnitudes obtained by expanding the boundary condition for the currents $J_g(z,t) = \sigma_{eff}(z,t)E(z,t)$ and identifying the terms associated to each temporal harmonic $e^{j\omega_i t}$.

This magnet-free graphene isolator can be integrated in arbitrarily small sizes (limited, of course, by spatial dispersion and fabrication processes). In addition, the operation frequency can be easily reconfigured through the same biasing network used to impart the spatiotemporal modulation, since all that is required is to change the 'static' component of the modulation voltages V_i to change the value of σ_s. The modulation period can also be changed easily if the discretization of the gates is fine enough, further increasing the flexibility of this platform. The downside of this type of isolator is its reliance of high-quality graphene, narrow bandwidth, and the relatively high modulation frequency required [21].

III. PLASMONIC ISOLATOR BASED ON INTERBAND TRANSITIONS

Here we explore a different approach to realize plasmonic isolation over graphene plasmonic waveguides, with important advantages over the previously presented device based on asymmetric bandgaps, at the cost of increased complexity. Graphene's modulation will now be used to couple otherwise orthogonal modes in a multimode structure, so that in the isolated direction all power is converted to a different mode at a different frequency, which can then be filtered or scattered [1, 5, 9]. In the connected direction, phase matching does not hold and thus no conversion occurs. The main advantages are smaller values of β_m, the ability to engineer a desired bandwidth, and potentially smaller insertion loss.

The structure under consideration is depicted in Fig. 2a and consists of a parallel plate graphene waveguide where one of the graphene layers can be biased independently. This type of structure could also be used to implement the isolator of the previous section, as the concept of asymmetric bandgaps is completely general. Note that for the present isolator only one of the sheets should be modulated, as the modulation profile must be asymmetric in the transverse plane in order to couple orthogonal modes [1,5]. The operation of the present isolator is illustrated in Fig. 2b. We refer to this type of mode conversion as an 'interband photonic transition' in analogy with electron transitions between bands in semiconductors [1]. Importantly, full power exchange between modes propagating in the same direction occurs periodically, with a period equal to the so-called coherence length, $L_c = \pi/2|\kappa|$, where κ is the coupling coefficient that describes how strongly the fields of even and odd overlap.

A convenient approach to study this problems is based on the coupled mode formalism [31,35]. This framework is inherently approximate but provides accurate results for most practical scenarios as well as deep physical insight. Coupled mode theory (CMT) describes the space or time evolution of overlapping modes in coupled resonators or waveguides, and it has been extensively used to model couples, filters, and more recently nonreciprocal acoustic and electromagnetic devices based on spatiotemporal modulation [1,5,36]. For two waves with amplitudes a_1 and a_2 traveling along the z-direction with propagation constants k_{z1} and k_{z2}, weakly coupled by a perturbation in z with period $p = 2\pi/\beta_m$, their coupled mode equations in space may be written as

$$\begin{aligned} \frac{da_1}{dz} &= -jk_{z1}a_1 + \kappa_{12}a_2 e^{j\Delta k_z}, \\ \frac{da_2}{dz} &= -jk_{z2}a_2 + \kappa_{21}a_1 e^{j\Delta k_z}. \end{aligned} \tag{6}$$

where $\Delta k_z = k_{z2}(\omega_0 \pm \omega_m) - k_{z1}(\omega_0) - \beta_m$. If the modes do not interact, $\kappa_{ij} = 0$ (with $i \neq j$), then the decoupled equations simply describe the amplitude variation given by the propagation constants k_{zi}. For coupled modes, the coupling coefficients κ_{ij} determine the rate with which the modes exchange power and, if power is to be conserved, $\kappa_{12} = \kappa_{21}^* = \kappa$ [35]. This operation is typically mediated by a z-periodic perturbation to the permittivity, so that the total permittivity becomes $\varepsilon = \varepsilon(x,y) + \delta\varepsilon(x,y,z,t)$. Because the perturbation $\delta\varepsilon(x,y,z,t)$ is periodic in space and time, it can be expanded as a Fourier series

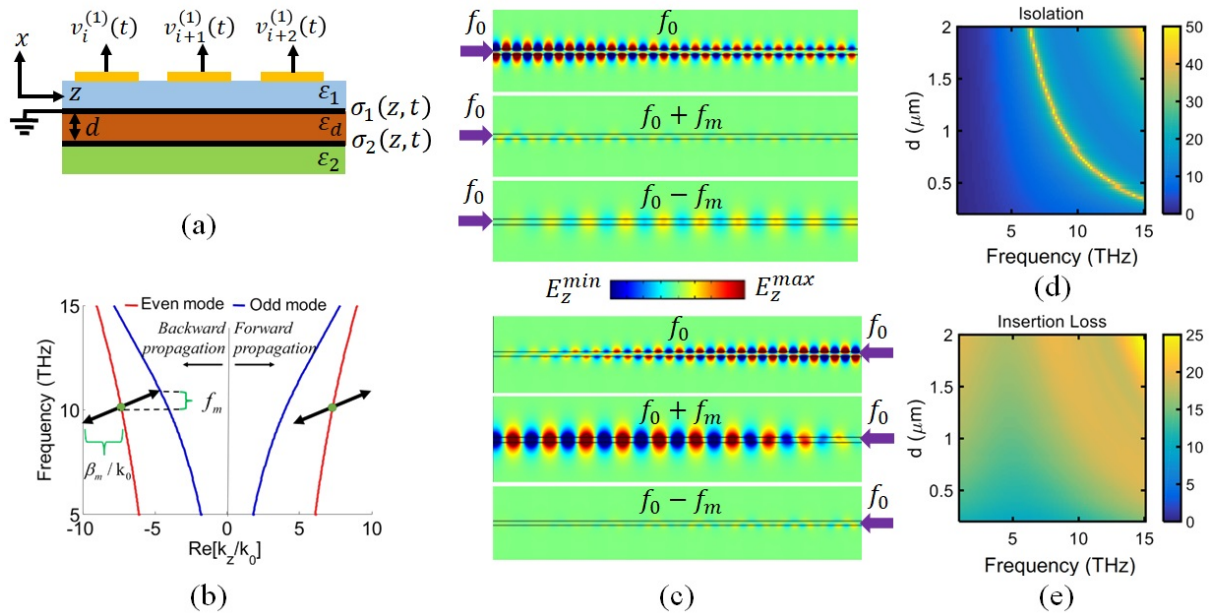

Figure 2. Graphene plasmonic isolator based on interband transitions. (a) Schematic of a graphene parallel-plate waveguide. The conductivity of the top layer is controlled along the z-axis using gating pads (in yellow) that are time-modulated. (b) Dispersion diagram. When the linear momentum provided by the spatiotemporal modulation (black arrow) fulfills that $\omega_m = \omega_2 - \omega_1$ and $\beta_m = k_2 - k_1$, perfect phase matching occurs and then total power conversion occurs between the orthogonal modes. This happens only in one direction. (c) Electric field (z-component) at the three frequencies involved in the device for both excitation directions at frequency 10THz. Other parameters are a modulation depth M = 0.1 and $d = 1\mu m$. (d) Maximum realizable isolation and (e) associated insertion loss, computed using coupled mode theory, for different operation frequencies and distance between graphene sheets, for a chemical potential $\mu_c = 0.5$ eV and $\tau = 0.5$ ps.

$$\delta\varepsilon = \sum_{n\neq 0} \varepsilon_n(x,y) e^{-jn(k_m z - \omega_m t)}, \tag{7}$$

where $n = 0$ is not included because of the definition of ε above. The coupling coefficient between two modes with field profiles $\bar{E}_1(x,y)$ and $\bar{E}_2(x,y)$ due to the n^{th} Fourier component of the perturbation is then defined as [32, 35]

$$\kappa_{12}^{(n)} = -\frac{j\omega}{4} \iint \varepsilon_n(x,y) \bar{E}_1(x,y) \bar{E}_2(x,y) dxdy, \tag{8}$$

where $\bar{E}_i$ must be normalized to a power flow of 1 Watt/m^2 along $\hat{z}$, i.e., $\iint \vec{E}_i \times \vec{H}_i^* dxdy = 2\ (W/m^2)$. Note that, in the simple scenario where $\delta\varepsilon(x,y,z,t) = \delta\varepsilon(x,y)\cos(\omega_m t - \beta_m z)$, there is only one term in the Fourier expansion, $\varepsilon_1 = \delta\varepsilon(x,y)$, resulting in one coupling coefficient $\kappa_{12}^{(1)} = \kappa_{21}^{(1)} = \kappa$. If κ can be computed, any non-reciprocal electromagnetic device based on linear or angular momentum bias can be designed and analyzed [1]. The platform explored here relies on modulating graphene's conductivity, not a permittivity. However, an equivalent way to describe a graphene sheet with conductivity σ_g is by considering it as an ultra-thin slab with thicknes $t_g \ll \lambda$ and permittivity ε_g [37]

$$\varepsilon_g = \varepsilon_0 - j\frac{\sigma_g}{\omega t_g}. \tag{9}$$

The equivalent permittivity of a graphene sheet under the modulation of Eq. (30) can thus be expressed as

$$\varepsilon_g(z,t) \approx -j\frac{\sigma_g}{\omega t_g}\left(1 + \frac{M}{2}e^{-j(\beta_m z - \omega_m t)} + \frac{M}{2}e^{+j(\beta_m z - \omega_m t)}\right), \tag{10}$$

where the term associated to the free-space permittivity can be neglected as it is orders of magnitude smaller than $j\frac{\sigma_g}{\omega t_g}$. Comparing with Eq. (7), we find

$$\varepsilon_{\pm 1} = \frac{M}{2}\frac{j\sigma_g}{\omega t_g}. \tag{11}$$

The coupling integral in Eq. (8) could now be solved using this permittivity and the corresponding fields inside and outside the equivalent graphene slab. However, rather than working with graphene's equivalent permittivity, it would far more convenient to use its conductivity, as this is usually a better way to solve graphene electromagnetic problems, both analytically and numerically. Integrating over the waveguide cross-section in the $t_g \to 0$ limit, we can write

$$\kappa_{21} = \frac{M}{8}\int \sigma_g \bar{E}_1^{(t)} \bar{E}_2^{(t)*} dy, \tag{12}$$

where $\bar{E}_i^{(t)}$ is the electric field tangential to graphene. Note that, since graphene lies in the x-z plane, the integral along the x axis is only non-zero at graphene's position, and the double integral has become a single integral along y, for the fields tangential to graphene. If we further assume a y-invariant graphene sheet, it simplifies to

$$\kappa_{21} = \frac{M}{8}\sigma_g \bar{E}_1^{(t)} \bar{E}_2^{(t)*}. \tag{13}$$

Compared to Eq. (8), the fields $\bar{E}_i$ must be replaced by their tangential components $\bar{E}_i^{(t)}$, because an infinitesimally thin conductive sheet cannot support currents along the perpendicular axis. Indeed, if the electromagnetic problem were instead solved within the equivalent thin-slab formalism, computing the fields "inside" graphene, one would find (for both TE and TM waves) strictly zero polarization current along the normal, and a non-zero uniform current in the tangential directions, providing fully consistent results. Therefore, the coupling coefficient between any two modes interacting with graphene is simply the dot product of the tangential electric fields on graphene, weighted by the perturbation to the conductivity. If several graphene sheets are present throughout the structure, interacting with the guided modes, all the contributions should be added. This derivation also clearly illustrates why the modulation must be asymmetric in the transverse plane: if both layers are identical and modulated in the same way, the even and odd symmetry of the modes would lead to the contributions perfectly cancelling out.

The implications of Eq. (12) are general and far-reaching, as it allows analytical treatment of any nonreciprocal device based on time-modulated graphene, including isolators, circulators, MTSs, or antennas, by simply solving the relevant eigenmodes, an approachable task even for non-analytical, complicated structures, solvable in a matter of seconds by any standard electromagnetic solver. In the case under study, the modes can fortunately be found analytically. They read [29, 38]:

Odd mode:

$$E_{z2} = Ae^{-jk_{x3}x}, \qquad E_{z1} = B\sin(k_{x1}x), \qquad E_{z3} = Ce^{jk_{x2}x}, \tag{14}$$

with

$$A = B\sin\left(\frac{k_{x1}d}{2}\right)e^{+\frac{jk_{x2}d}{2}}, \; C = -B\sin\left(\frac{k_{x1}d}{2}\right)e^{+\frac{jk_{x2}d}{2}}. \tag{15}$$

Even mode:

$$E_{z3} = Ae^{-jk_{x3}x}, \quad E_{z1} = B\cos(k_{x1}x), \quad E_{z2} = Ce^{jk_{x2}x}, \tag{16}$$

with

$$A = B\cos\left(\frac{k_{x1}h}{2}\right)e^{+\frac{jk_{x2}d}{2}}, \qquad C = -B\cos\left(\frac{k_{x1}h}{2}\right)e^{+\frac{jk_{x2}d}{2}}, \tag{17}$$

with media 1,2,3 numbered according to their relative permittivities shown in Fig 2a. The rest of field components can be retrieved through Maxwell's equations. Note that E_z is the only field component entering the computation of the coupling coefficient in Eq. (2), as $E_y = 0$ in both modes.

The amplitude evolution of the two modes through the waveguide can be computed using conventional CMT derivations [35]

$$A_1(z) = e^{\mathrm{Im}\left[k_z^{(\omega_0)}\right]z}e^{-j\Delta k/2}\left[\cos(zs) + j\,\frac{\Delta k/2}{s}\sin(zs)\right],$$
$$A_2(z) = e^{\mathrm{Im}\left[k_z^{(\omega_0\pm\omega_m)}\right]z}e^{j\Delta k/2}\,\frac{C\sin(zs)}{s}. \tag{18}$$

Note that for these expressions to be valid, the amplitude constants for both modes must be chosen so that the total power flow is equal to 1 Watt/m^2 along $\hat{z}$, i.e., $\iint \vec{E}_i \times \vec{H}_i^* dxdy = 2\ \mathrm{W/m^2}$, as stated earlier . Those amplitudes are then the ones entering in Eq. (12).

Figure 2c-e shows the response of an isolator with interlayer distance of d=1 μm designed to operate at 10 THz, with graphene's chemical potential $\mu_c = 0.5$ eV, modulation frequency $f_m = 100$ GHz, $M = 0.1$ and $\beta_m = 6.61 \cdot 10^5$ rad/m. Device length is equal to the coherence length for this specific modulation, $L_c = 58.4\ \mu m$ [21]. Up to 30 dB of isolation is achieved in this scenario at the design frequency of 10 THz, as most energy is converted to the even mode at $f_0 + f_m$ when the device is excited from the right (see Fig. 2c). Ideally, zero mode conversion would occur when exciting from the left port, since even and odd modes are not phase matched then, but the modes' finite linewidth leads to a small amount of undesired coupling to $f_0 - f_m$, visible in the left side of Fig. 2c. Such mode conversion can be considered a form of loss, as the converted power cannot reach the other port at the frequency and mode of interest. Like in the bandgap-based plasmonic isolator, this simulation was performed in COMSOL Multiphysics by coupling full-wave models at different frequency harmonics while taking into account the frequency-dispersive characteristics of graphene conductivity. Another requirement for efficient mode conversion is that both modes should have similar decay rates [1,21], so there are optimal combinations of substrates, interlayer spacing and chemical potential that also depend on frequency. Fortunately, the theoretical framework developed here allows to quickly compute with excellent accuracy all relevant performance metrics, enabling fast optimization of the numerous degrees of freedom in the structure. This is illustrated in Fig. 2d-e, which show the maximum possible isolation and associated insertion loss versus graphene interlayer separation and design frequency, for fixed values of $\mu_c = 0.5$ eV and $\varepsilon_r = 1$. Infinite isolation is possible in the limited part of the parameter space where both modes have identical decay rates, whereas the dependence with insertion loss is more complicated but can be efficiently optimized for any given specification. In this particular example, one could choose a design with lower insertion loss (bottom left part of the colormaps) by sacrificing perfect isolation.

IV. HYBRID GRAPHENE-DIELECTRIC ISOLATOR

Previous Sections explored the possibilities enabled by spatiotemporally modulated graphene to realize miniaturized, reconfigurable nonreciprocal plasmonic devices at THz frequencies. This platform does not rely on magneto-optic effects and it can thus be integrated with the myriad exciting graphene devices developed by the scientific community. Its major downside is that it requires relatively high-quality graphene able to support plasmons with low damping rates. Low damping is of course necessary for devices with low insertion loss, but there are also higher order effects exclusive the spatiotemporally modulated structures. Nonreciprocity through spatiotemporally modulation, whether implemented at

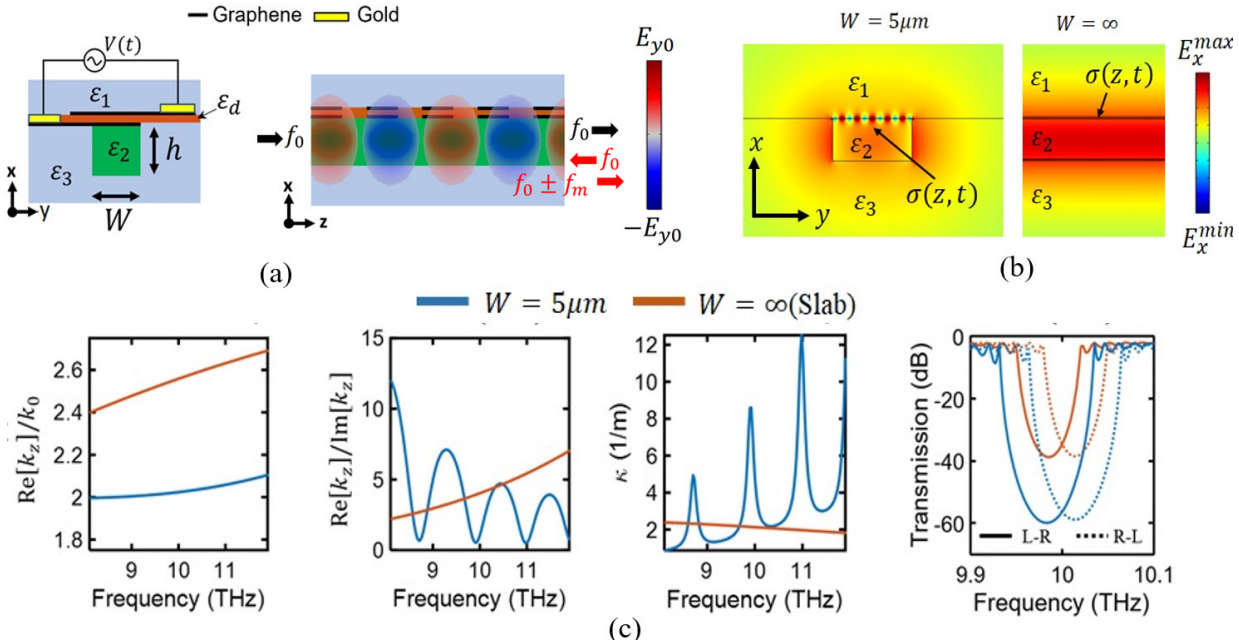

Figure 3. Photonic isolator based on spatiotemporally-modulated graphene coupled to a photonic waveguide. (a) Cross-section of a dielectric waveguide of width W and height h loaded by time-modulated graphene capacitors, left panel, which serves as a building block for realistic hybrid silicon-graphene non-reciprocal devices. (b) x-component of the electric field excited in the photonic waveguide considering that it has an infinite width (i.e., a slab), left panel, and finite width of $W = 5\mu m$, right panel. Results are computed using numerical simulations at 10 THz. (c) Electromagnetic response of the proposed isolator considering waveguide with infinite (red line) and finite (blue) width. Left: phase constant, $Re[k_z]$, normalized by the free-space wavenumber, k_0. Central-left: figure of merit, $Re[k_z]/Im[k_z]$. Central-right: coupling coefficient, κ. Right: transmission through the structure when excited from left (solid lines) and right (dashed lines) ports. Other parameters are $\mathrm{h} = 2.75\ \mu\mathrm{m}, \mu_c = 0.4\ \mathrm{eV}, \tau = 1\ \mathrm{ps}, \varepsilon_1 = \varepsilon_3 = 4, \epsilon_d = 9$ and $\varepsilon_2 = 12$.

microwaves, THz, or optics, always relies on carefully engineering some sort of interaction between modes through the modulation. The *spatial* part of the modulation is designed to phase-match the modes in order to maximize their interaction for some range of frequencies. The *temporal* part of the modulation then up-shifts the system's response for one propagation direction, and down-shifts it for the opposite one. Ideally, this results in some frequencies seeing a large contrast in the system's response for opposite propagation directions, and devices like isolators can be made for those frequencies. The behavior of such interactions versus frequency is therefore critical, and loss affects the frequency response of any system. For instance, in the bandgap-based isolators of Section II, increasing graphene's loss (by lowering the phenomenological relaxation time τ) would result not only in larger insertion loss but also in lower isolation, because the transition from zero reflection outside the bandgap (smaller $\mathrm{Im}[k_z(\omega)]$) to high reflection inside the bandgap (larger $\mathrm{Im}[k_z(\omega)]$) becomes smoother, and contrast for opposite directions decreases. As a general rule, devices based on modes with lower Q factor (more loss and larger spectral linewidth) require larger modulation frequencies to achieve the same asymmetry and isolation. Therefore, poor-quality graphene may require very high modulation speeds (large ω_m), increasing the cost and complexity of the biasing network. This may be especially challenging at increasingly high carrier frequencies (far and mid infrared), since what matters is the ratio between modulation frequency and carrier frequency. Such relation between loss and power exchange between modes is quite complex and appears in most devices based on spatiotemporal modulation [1].

To lessen the reliance on high-purity graphene, we explore in this Section an alternative technological platform that combines the fast modulation speed enabled by graphene with high quality-factor photonic modes in dielectric waveguides, exploiting the most attractive features of each platform. The resulting hybrid graphene-dielectric photonic devices are intrinsically silicon-compatible, more resilient to imperfections in graphene manufacturing processes, and can be scaled from THz to telecom wavelengths. Importantly, these devices are well suited for integrated silicon photonic systems, since they are just regular silicon waveguides to the outside world. This is possible because graphene is used *only* to engineer the required nonreciprocal coupling between photonic states, having a small effect on their dispersion and field profile.

Given the rapid growth of silicon photonics in recent years [39-44] as a promising solution to the interconnect bottlenecks in electronics, the platform and devices proposed in the following could have far reaching technological implications.

Consider the structure of Fig. 3a, where a pair of closely spaced graphene sheets separated by an insulator with permittivity ε_d has been transferred on top of a dielectric slab waveguide with permittivity ε_2 surrounded by media ε_1 and ε_3. For deeply subwavelength separation distance between the graphene sheets, the effective conductivity of the stack can be approximated as [24]

$$\sigma_{stack} \approx \sigma_1 + \sigma_2. \tag{19}$$

Applying a modulation voltage between them, the conductivity of the stack can easily be controlled broadly. A similar configuration, employing a single capacitor with a 65 nm Al_2O_3 insulating layer has been used to experimentally realize optical modulators with speeds as high as 30 GHz [23], limited mainly by suboptimal contact resistances. Speeds close to 100 GHz would be possible with state-of-the-art contacts, which would further boost the performance of the platform proposed here [44, 45,46]. Nonetheless, the isolator proposed in the following will use a conservative 30 GHz modulation frequency. In what follows, the stack will be modeled by its effective conductivity σ_{stack}. This description is justified for two reasons. First, the free-space wavelengths at the frequency ranges considered here, around 30 μm (10 THz), are much larger than a ~50 nm stack, so the approximation of subwavelength dimensions where the conductivities are added is reasonable [24,29]. Second, the actual value of ε_d has little effect on the overall electromagnetic response of the stack due to the thinness of the insulator and the highly inductive conductivity of graphene, which is equivalent to a very large negative real permittivity. For reference, a graphene monolayer with $\mu_c = 0.4$ eV, modelled as an equivalent dielectric slab of permittivity ε_g and thickness $t_g = 1$ nm, has a permittivity $\varepsilon_g = \varepsilon_0 - j\sigma/\omega t_g = -1350\varepsilon_0$ at 10 THz. It should also be noted, however, that the insulator's thickness and permittivity do play an important role in determining the capacitance and carrier density induced on graphene for a given bias voltage, as given by Eq. (1).

If multiple of these capacitors are placed along the propagation direction z of a waveguide, as shown in Fig. 3a, one can synthesize through well-known relations described in Section II the voltages required to yield a spatially and temporarily varying conductivity profile of the form

$$\sigma_{eff}(z,t) = \sigma_{stack}(1 + M \cdot cos(\omega_m t - \beta_m z)), \tag{20}$$

where σ_{stack} is given in Eq. (19). Even though it essentially has the same form as Eq. (3), except for σ_{stack}, the underlying modulation parameters like voltage or oxide capacitance will in general be different. Note that the required modulation depth is smaller than in the experimentally-demonstrated modulators from [23], as those devices require large voltage swings to switch critical coupling on and off, whereas the devices proposed here work even for small modulation depths. However, larger modulation depths may still be useful to increase coupling strength and therefore achieve more compact devices, although this requires larger bias voltages and may potentially introduce spurious couplings. It is worth emphasizing again that imperfections in the modulation scheme or graphene are not expected to significantly affect device performance, since information does not travel as currents in graphene but along the dielectric waveguide.

Let us consider an isolator based on asymmetric bandgaps like that discussed in Section II, but now using a hybrid graphene-dielectric slab waveguide instead of a graphene-only, plasmonic one. We will examine two different configurations: a dielectric slab that admits a fully analytical treatment [22], aiming to obtain valuable intuition on the underlying physics; and a finite width waveguide that can be implemented in practice. The latter case is a challenging problem from a modelling perspective, since simple closed-form expressions for the modal fields and dispersion relation are not available even in the unmodulated case. Harmonic-balance full-wave simulations of the full isolator are not feasible either, since several coupled harmonic modules must be solved simultaneously for a structure that is electrically very large. The only feasible approach is based on CMT, whose accuracy was recently validated for the slab case [22]. To this end, it is required to obtain (i) the dispersion of the hybrid TE/TM mode; and (ii) the normalized tangential electric fields on the graphene stack, so that Eqs. (7) and (13) can be applied. Fortunately, this can be numerically computed in an electromagnetic eigenmode solver for the transverse section of the waveguide, for instance in COMSOL Multiphysics. Fig. 4 shows the electric field components for a finite waveguide with $W = 5\ \mu m$ and otherwise identical parameters to the isolator of Fig. 3, with and without the presence of the graphene stack. The first thing worth mentioning is that the mode is predominantly TE for this geometry, as the transverse component of the electric field (E_y) is much stronger than the longitudinal one (E_z). The propagation constant, k_z, is barely affected by the presence of graphene, but the field distribution is noticeably altered in the vicinity of graphene due to transverse Fabry Perot plasmonic resonances. This is a

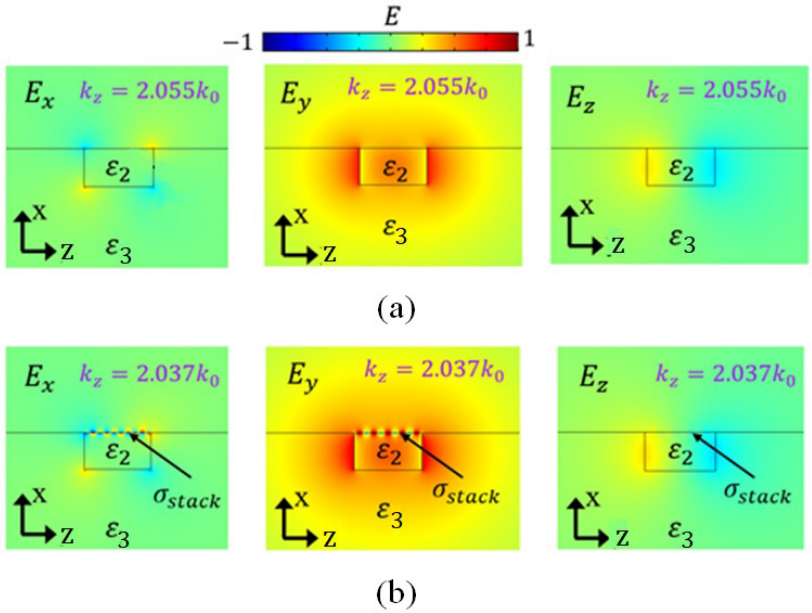

Figure 4. Electric field components of fundamental hybrid TE/TM mode in a dielectric waveguide without (a) and with (b) a graphene stack perturbing the mode, as shown in Figure 3. All panels are on the same color scale. Propagation constant k_z is barely affected, but fields are strongly concentrated on the graphene stack due to a Fabry Perot resonance. All parameters are as in Figure 3.

remarkable result, as the mode mainly propagates along the dielectric regions but there are strongly enhanced fields on graphene that will ultimately allow for stronger coupling, as dictated by Eq. (13). This is demonstrated in Fig. 3c, which shows the dispersion, coupling coefficient κ, and isolation for the infinite and finite modulated waveguides. In the slab scenario, the dependence of all parameters is monotonic because an infinite graphene stack cannot support Fabry Perot resonances. As usual, the real part of k_z is smaller in a finite waveguide than in the slab, because more energy travels in the low-ε material. More interesting is the behavior of the figure of merit, $\mathrm{Re}[k_z]/\mathrm{Im}[k_z]$, and κ. Due to the Fabry Perot resonances of surface waves in the graphene stack, there are clear maxima and minima of κ. The points of maximum κ correspond exactly to the points of minimum $\mathrm{Re}[k_z]/\mathrm{Im}[k_z]$, which is expected given that fields are more strongly concentrated in the graphene area (which is more lossy) when coupling between graphene and the dielectric mode is maximum. This does not mean, however, that a finite-waveguide isolator will have larger insertion loss than predicted by the slab model, even if $\mathrm{Im}[\mathrm{k_z}]$ is larger (in absolute or relative terms to $\mathrm{Re}[\mathrm{k_z}]$). The reason is that larger κ also implies a shorter device for a given isolation, so the factor $\exp(-\mathrm{Im}[k_z]\cdot L)$, which loosely approximates loss, may be smaller. Alternatively, *M* may be reduced while maintaining a fixed κ if one operates at a resonance. For instance, around 11 THz, κ is six times larger in the finite waveguide, which would roughly translate to requiring modulation depths *M* six times smaller than anticipated by the slab calculations. This may be a very attractive approach since it would drastically decrease the bias voltages. For the sake of comparison, Fig. 3c (righ panel) shows the bidirectional transmission of an isolator hosted by this waveguide, with the same modulation depth $M = 0.3$ and device length L=1.5 μm and compare it to the slab case. Because κ is much larger around 10 THz, transmission contrast and thus isolation is more than 20 dB larger, achieving levels over 50 dB. Clearly, the device could be made shorter or *M* smaller to achieve an isolation comparable to the slab waveguide.

V. CONCLUSION

In summary, we have exploited the spatiotemporal modulation of graphene's conductivity to put forward a promising platform to realize isolators at terahertz and infrared frequencies without reliance on magneto-optic effects in structures fully compatible with integrated technology. First, we have focused on plasmonic isolators, based on various mechanisms such as asymmetric bandgaps and interband transition, and we have developed theoretical frameworks to analyze and efficiently design them. We have reported, and validated using full-wave numerical simulations, very promising performance with isolation levels over 30 dB. The major challenge faced by this first approach is the need of high-quality graphene able to support plasmons with low damping. To overcome this shortcoming, we have introduced a hybrid

platform that combines high-Q modes on dielectric waveguides with spatiotemporally modulated graphene. In particular, we have exploited for the very first time transversal Fabry-Perot resonance that appears due to the hybridization between graphene and the finite-width waveguide to significantly increase the coupling between the modes, boosting the isolation levels over 50 dB, reducing the overall length of the device, and reducing the voltages level required by the feeding network. Such properties address important challenges of the state of the art in terms of CMOS-compatibility, integration, miniaturization, losses, and performance. The versatility and far-reaching implications of the proposed approach should be emphasized: it can in principle be employed to develop low-loss photonic circulators, Faraday rotators, nonreciprocal leaky wave antennas, as well as to manipulate nonreciprocity at the micro/nano scale to realize advanced functionalities such as nonreciprocal beam-steering and lensing. In addition, its performance at infrared frequencies makes this platform a good candidate to engineer nonreciprocal emission and absorption in thermal management applications where efficiency is critical, for instance by preventing an absorber from re-radiating energy in thermophotovoltaic cells.

ACKNOWLEDGMENTS

This work was supported by the National Science Foundation with CAREER Grant No. ECCS-1749177. Authors thank Prof. D. Sounas (Wayne State University), Prof. A. Alù (City University of New York) and Prof. A. Knoesen (University of California, Davis) for fruitful discussions.

REFERENCES

[1] Sounas, D. L., and Alù, A., "Non-reciprocal photonics based on time modulation," Nat. Photonics 11(12), 774–783 (2017).

[2] Estep, N. A., Sounas, D. L., and Alu, A., "Magnetless microwave circulators based on spatiotemporally modulated rings of coupled resonators," IEEE Trans. Microw. Theory Tech. 64(2), 502–518 (2016).

[3] Fleury, R., Sounas, D. L., Sieck, C. F., Haberman, M. R., and Alù, A., "Sound isolation and giant linear nonreciprocity in a compact acoustic circulator," Science 343(6170), 516–519 (2014).

[4] Kord, A., Sounas, D. L., and Alù, A., "Magnet-less circulators based on spatiotemporal modulation of bandstop filters in a delta topology," IEEE Trans. Microw. Theory Tech. 66(2), 911–926 (2018).

[5] Yu, Z. and Fan, S., "Complete optical isolation created by indirect interband photonic transitions," Nat. Photonics. 3(2), 91–94 (2009).

[6] Qin, S., Xu, Q., and Wang, Y. E., "Nonreciprocal components with distributedly modulated capacitors," IEEE Trans. Microw. Theory Tech. 62(10), 2260–2272 (2014).

[7] Shi, Y., Han, S., and Fan, S., "Optical circulation and isolation based on indirect photonic transitions of guided resonance modes," ACS Photonics 4(7), 1639–1645(2017).

[8] Taravati, S, "Self-biased broadband magnet-free linear isolator based on one-way space-time coherency," Phys. Rev. B 96(23), 235150 (2017).

[9] Lira, H., Yu, Z., Fan, S., and Lipson, M., "Electrically driven nonreciprocity induced by interband photonic transition on a silicon chip," Phys. Rev. Lett. 109(3), 1–5 (2012).

[10] Chamanara, N., Taravati, S., Deck-Léger, Z. L., and Caloz, C., "Optical isolation based on space-time engineered symmetric photonic band gaps," Phys. Rev. B 96, 155409 (2017).

[11] Wu, X., Liu, X., Hickle, M. D., Peroulis, D., Gomez-Diaz, J. S., and Alvarez-Melcon, A., "Non-reciprocal bandpass filters using time-modulated resonators," IEEE Trans. Microw. Theory Tech., in press.

[12] Alvarez-Melcon, A., Wu, X., Zang, J., Liu, X., and Gomez-Diaz**,** J. S., "Coupling Matrix Representation of Nonreciprocal Filters Based on Time Modulated Capacitors," under review.

[13] Hadad, Y., Soric, J. C., and Alù, A., "Breaking temporal symmetries for emission and absorption," Proc. Natl. Acad. Sci. USA 113, 3471 (2016).

[14] Taravati, S., and Caloz, C., "Mixer-duplexer-antenna leaky-wave system based on periodic space-time modulation," IEEE Trans. Antennas Propag. 65, 442 (2017).

[15] Zhang, J., Correas-Serrano, D., Do, J. T. S., X. Liu, Alvarez-Melcon, A., and Gomez-Diaz, J. S., "Nonreciprocal wavefront engineering with time-modulated gradient metasurfaces," Physical Review Applied (in press).

[16] Almeida, V. R., Barrios, C. A., Panepucci, R. R., and Lipson, M., "All-optical control of light on a silicon chip," Nature 431, 1081 (2004).

[17] Xu, Q., Schmidt, B., Shakya, J., and Lipson, M., "Cascaded silicon micro-ring modulators for WDM optical interconnection", Opt. Express 14, 9431 (2006).

[18] Lira, H., Yu, Z., Fan, S., and Lipson, M., "Electrically driven nonreciprocity induced by interband photonic transition on a silicon chip," Phys. Rev. Lett 109 (3), 1–5 (2012).

[19] Castro Neto, A.H., Guinea, F., Peres, N. M. R., Novoselov, K. S., and Geim, A. K. "The electronic properties of graphene," Rev. Mod. Phys. 81(1), 109–162 (2009).

[20] Koppens, F. H. L., Chang, D. E., and García de Abajo, F. J., "Graphene plasmonics: A platform for strong light-matter interactions," Nano Lett. 11, 3370–3377 (2011).

[21] Correas-Serrano, D, Gomez-Diaz, J. S., Sounas, D. L., Hadad, Y., Alvarez-Melcon, A., and Alù, A., "Nonreciprocal graphene devices and antennas based on spatiotemporal modulation," IEEE Antennas Wireless Propag. Lett. 15, 1529 (2016).

[22] Correas-Serrano, D., Alu, A. and Gomez-Diaz, J. S., "Magnetic-free nonreciprocal photonic platform based on time-modulated graphene," Phys. Rev. B 98, 165428 (2018).

[23] Phare, C. T., Daniel Lee, Y. H., Cardenas, J., and Lipson, M., "Graphene electro-optic modulator with 30 GHz bandwidth," Nat. Photonics 9(8), 511–514 (2015).

[24] Gomez-Diaz, J. S., Moldovan, C., Capdevilla, S., Bernard, L. S., Romeu, J., Ionescu, A. M., Magrez, A., and Perruisseau-Carrier, J., "Self-biased Reconfigurable Graphene Stacks for Terahertz Plasmonics," Nat. Commun. 6, 6334 (2015).

[25] Gomez-Diaz, J. S., and Alù, A., "Flatland optics with Hyperbolic Metasurfaces," ACS Photonics 3(12), 2211–2224 (2016).

[26] Paul, N. K., Correas-Serrano, D., and Gomez-Diaz, J. S., "Giant lateral optical forces on Rayleigh particles near hyperbolic and extremely anisotropic metasurfaces," Phys. Rev. B 99(12), 121408 (2019).

[27] Woessner, A., Lundeberg, M.B., Gao, Y., Principi, A., Alonso-González, P., Carrega, M., Watanabe, K., Taniguchi, T., Vignale, G., Polini, M. and Hone, J., "Highly confined low-loss plasmons in graphene–boron nitride heterostructures," Nat. Mater. 14(4), 421–425 (2014).

[28] Ruesink, F., Miri, M. A., Alù, A., and Verhagen, E., "Nonreciprocity and magnetic-free isolation based on optomechanical interactions," Nat. Commun. 7, 13662 (2016).

[29] Correas-Serrano, D., Gómez-Díaz, J. S., Perruisseau-Carrier, J., and Álvarez-Melcón, A., "Spatially dispersive graphene single and parallel plate waveguides: Analysis and circuit model," IEEE Trans. Microw. Theory Tech. 61(12), 4333–4344 (2013).

[30] Correas-Serrano, D., Gómez-Díaz, J. S., Perruisseau-Carrier, J., and Alvarez-Melcon, A., "Graphene-based plasmonic tunable low-pass filters in the terahertz band," IEEE Trans. Nanotechnol. 13(6), 1145–1153 (2014).

[31] Forati, E., and Hanson, G. W., "Soft-boundary graphene nanoribbon formed by a graphene sheet above a perturbed ground plane: conductivity profile and SPP modal current distribution," J. Opt. 15(11), 114006 (2013).

[32] Yariv, A., and Yeh, P., [Optical waves in crystals: Propagation and Control of Laser Radiation], Wiley, New York, 1984.

[33] Oliner, A. A., and Hessel, A., "Guided waves on sinusoidally-modulated reactance surfaces," IRE Trans. Antennas Propag. 7(5), 201–208 (1959).

[34] Jackson, J. D., [Classical Electrodynamics], Wiley Online Library, 1975.

[35] Haus, H. A., [Waves and Fields in Optoelectronics], Prentice-Hall, 1984.

[36] Sounas, D. L., Caloz, C., and Alù, A., "Giant non-reciprocity at the subwavelength scale using angular momentum-biased metamaterials," Nat. Commun. 4, 2407 (2013).

[37] Vakil, A., and Engheta, N., "Transformation optics using graphene," Science, 332(6035), 1291–1294 (2011).

[38] Hanson, G. W., "Quasi-transverse electromagnetic modes supported by a graphene parallel-plate waveguide," J. Appl. Phys. 104(8), 084314 (2008).

[39] Jalali, B., and Fathpour, S., "Silicon photonics," J. Light. Technol. 24(12), 4600–4615 (2006).

[40] Khanikaev, A. B., and Alù, A., "Silicon photonics: One-way photons in silicon," Nat. Photonics 8(9), 680–682 (2014).

[41] Hochberg, M., and Baehr-Jones, T., "Towards fabless silicon photonics," Nat. Photonics 4(8), 492–494 (2010).

[42] Leuthold, J., Koos, C., and Freude, W., "Nonlinear silicon photonics," Nat. Photonics 4, 535–544 (2010).

[43] Soref, R., "Mid-infrared photonics in silicon and germanium," Nat. Photonics 4(8), 495–497 (2010).

[44] Soref, R., "The past, present, and future of silicon photonics," IEEE J. Sel. Top. Quantum Electron. 12(6), 1678–1687 (2006).

[45] Leong, W. S., Gong, H., and Thong, J. T. L., "Low-contact-resistance graphene devices with nickel-etched-graphene contacts," ACS Nano 8(1), 994–1001 (2014).

[46] Li, W., Liang, Y., Yu, D., Peng, L., Pernstich, K.P., Shen, T., Hight Walker, A.R., Cheng, G., Hacker, C.A., Richter, C.A. and Li, Q., "Ultraviolet/ozone treatment to reduce metal-graphene contact resistance," Appl. Phys. Lett. 102(18), 183110 (2013).